MRS Advances
https://doi.org/10.1557/s43580-023-00600-7

ORIGINAL PAPER

Nanoscale characterizations of mineralized piezoelectric scaffolds

Nathanial Buettner[1] · Grant Kitchen[2] · Mostafa Omar[3] · Bohan Sun[3] · Haklae Lee[1] · Sung Hoon Kang[3] · Ange-Therese Akono[1]

Received: 31 March 2023 / Accepted: 31 May 2023

Abstract

Inspired by the mineralization process of bone, we have investigated mineralization on piezoelectric samples immersed in a solution with mineral ions. We have utilized polyvinylidene fluoride as a piezoelectric material and 10× simulated body fluid as a mineral solution. Three synthetic material systems were developed and characterized using scanning electron microscopy, X-ray diffraction, nanoindentation, and scratch testing. With these techniques, we provide insights into how the characteristics of the mineralization protocol affect the microstructure, chemical composition, crystal structure, and mechanical properties of the minerals. Increasing the solution temperature from 25 to 50 °C resulted in a greater packing density, roughly 10 times the stiffness and 4 times the fracture toughness. Collagen surface treatment resulted in roughly 7 times the stiffness along with potential anisotropy in the fracture toughness. Lastly, calcium phosphate minerals appear to pack in low-density and high-density phases on the piezoelectric scaffolds.

Introduction

The remarkable self-adaptive mechanical properties and self-regeneration abilities of bone provide inspiration for the development of next generation synthetic material systems [1]. When bone is mechanically stimulated, the negative peptide charges attract positively charged ions from the blood stream to generate calcium phosphate minerals. Previous studies demonstrate that minerals also preferentially deposit onto negatively charged surfaces in synthetic material systems in the presence of simulated body fluid (SBF), which mimics ion concentrations of blood [2, 3]. As such, piezoelectric materials, which generate electric charges in response to mechanical stimuli, have gained attention as scaffolds as they can show self-adaptive mechanical properties and self-regeneration abilities [4, 5].

The power of utilizing piezoelectric materials in this regard is that piezoelectric material combined with a source of materials like SBF can proportionally form minerals as a function of stress and repair damaged minerals. As piezoelectric materials proportionally generate electrical charges upon stress, the generated charges can attract ions from SBF and deposit minerals, accordingly, resulting in a self-adaptive behavior, similar to bone. In addition, if a part of the mineral layers is damaged, it exposes the underlying charges and can facilitate mineral formation on the area. Hence, these charges can act as signals for mineral formation based

✉ Sung Hoon Kang
shkang@jhu.edu

✉ Ange-Therese Akono
ange-therese.akono@northwestern.edu

Nathanial Buettner
nathanial.buettner@northwestern.edu

Grant Kitchen
gkitche1@jhu.edu

Mostafa Omar
momar5@jhu.edu

Bohan Sun
bsun22@jhu.edu

Haklae Lee
haklae.lee@northwestern.edu

[1] Department of Civil and Environmental Engineering, Northwestern University, 2145 Sheridan Road, Evanston, IL 60201, USA

[2] Department of Materials Science and Engineering, Johns Hopkins University, 3400 N. Charles Street, Baltimore, MD 21218, USA

[3] Department of Mechanical Engineering, Johns Hopkins University, 3400 N. Charles Street, Baltimore, MD 21218, USA

Published online: 27 June 2023

on the stress or damage. This makes them a good candidate for a number of applications [6].

Previously, piezoelectric materials have been used for biomedical applications by utilizing intrinsic charges on the material. For example, PVDF was used as a coating for titanium alloy surfaces in implants to improve their biological properties [7, 8]. In addition, piezoelectric scaffolds have been mineralized with calcium carbonate for bone tissue integration applications as well as for promoting osteogenic differentiation [9–12]. More recently, the piezoelectric charge generated as a response to mechanical loading was studied to synthesize mechanically self-adaptable composites which can autonomously enhance their mechanical properties based on loading conditions [4]. As seen in all the previous examples, mineralization on a piezoelectric material has been employed to enhance the reliability and biocompatibility of scaffolds and implants.

There are multiple factors affecting the growth and properties of the minerals formed on piezoelectric scaffolds in SBF besides the surface charges. For instance, the classical model of heterogeneous nucleation indicates the dependence of the nucleation rate on the temperature [13]. Furthermore, surface treatment with materials such as collagen can impact mineralization. Wang et al. demonstrated that collagen could initiate and orient the growth of calcium phosphates [14]. In general, what is not fully understood is the influence of temperature and surface treatment on the microstructure, chemical composition, and mechanical properties of the minerals formed on piezoelectric scaffolds in mineral solutions.

In this work, we have synthesized mineralized piezoelectric scaffolds using three protocols. We have utilized the piezoelectric properties of polyvinylidene fluoride (PVDF) to generate mineral coatings in SBF. Then, we have characterized the microstructure, chemical composition, crystal structure, and mechanical properties of the minerals using scanning electron microscopy, X-ray diffraction, nanoindentation, and scratch testing. Lastly, we discuss how the characteristics of the mineralization protocols affect the properties of the minerals.

Materials and methods

Materials synthesis

Commercially available, 110-µm-thick PVDF (Measurement Specialties, Inc.) was cut into 25 × 50 mm pieces. The edges of the pieces were sealed with low-friction polyether ether ketone tape (McMaster-Carr) to avoid leaving residue on the PVDF. A modified formulation of SBF called 10× SBF, with much higher ionic concentrations than human blood, was used to supply the mineral ions to the PVDF samples [15, 16]. This mineral solution was chosen over other formulations of simulated body fluid [17, 18] to accelerate the coating process so that full coatings were produced within two weeks.

PVDF samples were mineralized with three different protocols. The first two protocols involved placing the bare PVDF samples into 10× SBF at 25 °C (PVDF-25) or 50 °C (PVDF-50) for 2 weeks to induce mineral deposition. The third protocol involved pretreating the PVDF with collagen to investigate the effects of collagen on the minerals (PVDF-col). For this protocol, prior to mineralization, type I bovine collagen (Sigma-Aldrich) was mixed with phosphate-buffered solution and deposited onto both sides of the PVDF. The collagen solution was polymerized at 37 °C for 3 h. Then, the collagen-treated PVDF was placed into the 10× SBF at 25 °C for 2 weeks. For PVDF-25 and PVDF-col, the 10× SBF was refreshed every 24 h. For PVDF-50, the 10× SBF was refreshed every 48 h. Samples were rinsed thoroughly with deionized water after mineralization to remove any residual sodium chloride from the surface.

Scanning electron microscopy

Backscattered environmental scanning electron microscopy (SEM) was conducted using the FEI Quanta 650 environmental scanning electron microscope in low-vacuum mode at an accelerating voltage of 15 kV, a working distance of 10 mm, and for magnification levels of 200×, 1000×, and 5000×. Energy-dispersive X-ray spectroscopy (EDS) was also performed at these magnifications to investigate the chemical composition of the mineralized scaffolds.

X-ray diffraction

X-ray diffraction (XRD) analysis was used to characterize the crystal structures of the mineralized scaffolds. The analysis was performed using the Rigaku Smartlab 3 kW Gen2 diffractometer. The parameters used for the powder diffraction were an accessible energy of 40 keV, current of 35 mA, 2θ angle range of 10–75°, step size of 0.05°, and scan speed of 5 s/step.

Nanoindentation

The elasto-plastic behavior of mineralized scaffolds was probed using nanoindentation testing. The indentation modulus M and the indentation hardness H were measured by the application of the Oliver and Pharr method [19, 20]:

$$M = \frac{\sqrt{\pi}}{2}\frac{S}{\sqrt{A}}; \quad H = \frac{P_{max}}{A}, \tag{1}$$

where S is the unloading slope, P_{max} is the maximum vertical force, and A is the projected load-bearing contact area. The

nanoindentation tests were conducted using an Anton Paar nanoHardness tester. Prior to testing, the Berkovich indenter was calibrated with fused silica. In our load-controlled tests, the maximum force, P_{max}, was 300 μN, the loading/unloading rate was 1200 μm/min, and the holding phase lasted 5 s. Load-controlled nanoindentation was only performed successfully for PVDF-50 and PVDF-col. Given the softness of PVDF-25, depth-controlled nanoindentation was performed with a maximum depth of 1000 nm, loading/unloading rate of 2000 nm/min, and holding phase of 10 s.

Statistical deconvolution analysis

The local packing density, η_i, was determined for PVDF-50 and PVDF-col using theoretical solutions for indentation in porous cohesive frictional materials [21]:

$$M_i = m_s \mathcal{M}(\eta_i, \nu_s); \quad H_i = c_s \mathcal{H}(\eta_i, \alpha_s, \nu_s), \tag{2}$$

where m_s, ν_s, c_s, and α_s are the plane strain elastic modulus, Poisson's ratio, cohesion, and coefficient of internal friction of the solid skeleton, respectively. $\mathcal{M}$ and $\mathcal{H}$ are the indentation modulus linear upscaling and indentation hardness nonlinear upscaling functions, respectively, which are determined using nonlinear optimization in Python [22].

Using the indentation modulus, indentation hardness, and local packing density, statistical deconvolution analyses were performed to identify the chemomechanical phases that are present in the minerals. This technique has been used to characterize the phases of heterogeneous materials [23, 24]. In this analysis, it is assumed that each phase j is characterized by the surface fraction f_j, the mean indentation modulus μ_j^M, indentation hardness μ_j^H, and local packing density η_j, and the standard deviation of the indentation modulus s_j^M, indentation hardness s_j^H, and local packing density s_j^η. To determine these mechanical parameters, the squared sum difference of the experimental cumulative distribution functions $F_X(X_i)$ and weighted model cumulative distribution functions $F(X_i, \mu_j^X, s_j^X)$ were minimized:

$$\min \sum_{i=1}^{N} \sum_{X=(M,H,\eta)} \left(\sum_{j=1}^{n} f_j F(X_i, \mu_j^X, s_j^X) - F_X(X_i) \right)^2. \tag{3}$$

The minimization was constrained by requiring the sum of the surface fractions of each phase to be equal to one $\sum_{j=1}^{n} f_j = 1$. Moreover, to clearly distinguish the phases that are present in the minerals, the following constraint was provided:

$$\mu_j^X + s_j^X \leq \mu_{j+1}^X - s_{j+1}^X. \tag{4}$$

Scratch testing

The fracture response of the mineralized scaffolds was characterized using scratch testing. Scratch testing involves pushing a sphero-conical probe across the surface of a material under a prescribed linearly increasing vertical load. The horizontal force F_T and penetration depth d were measured and used to calculate the fracture toughness K_c [25]:

$$K_c = \frac{F_T}{\sqrt{2pA}}, \tag{5}$$

where $2pA$ is the scratch probe shape function, which was calibrated prior to testing using fused silica as a reference material [26]. Scratch tests were conducted with an Anton Paar microScratch tester. The scratch probe was a Rockwell C diamond probe with a tip radius of $R = 200$ μm and a half-apex angle of 60°, the prescribed maximum vertical force was 300 mN (for PVDF-col) and 500 mN (for PVDF-25 and PVDF-50), the scratch length was 3 mm, and the scratch speed was 6 mm/min. Scratch testing was performed in two directions (parallel to the front edge of the scaffold (X1) and perpendicular to the front of the scaffold (X2)) for PVDF-col to account for potential anisotropy [27].

Results

Microstructure and chemistry

The mineralization conditions affect the morphology and the packing density of the minerals. The vast majority of the PVDF was covered by each of the three mineralization protocols (Fig. B1 in the Supplementary Material). Figure 1 depicts SEM images of PVDF-25, PVDF-50, and PVDF-col at magnifications of 200×, 1000×, and 5000×. PVDF-25 has a porous coating of spherical minerals that are aggregated into bundles. PVDF-50 has a denser packing than PVDF-25, consisting of both spherical minerals and larger prismatic crystals. Compared to PVDF-25 and PVDF-50, PVDF-col exhibits a starkly different microstructure, consisting of a fragmented coating of mineralized collagen. The minerals are pancake-like and more densely packed and larger than that of PVDF-25 and PVDF-50.

Furthermore, the mineralization conditions are suggested by SEM-EDS (Tables B1–B3 and Figs. B2–B10) to affect the chemical composition of the precipitated minerals. Oxygen, calcium, phosphorus, carbon, and fluorine were detected in PVDF-25 and PVDF-50. Compared to PVDF-25, PVDF-50 has a much greater relative amount of carbon. Oxygen, calcium, phosphorus, and carbon were detected in PVDF-col, while the fluorine in the PVDF was not detected.

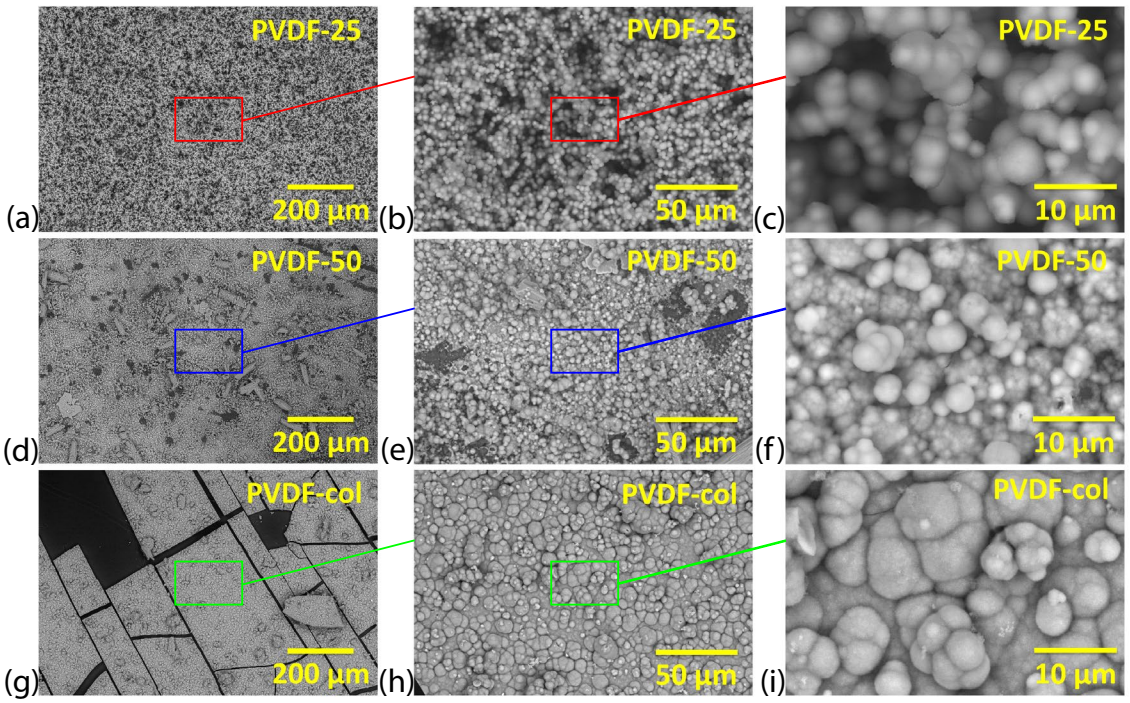

Fig. 1 SEM images of PVDF-25 at magnifications of **a** 200×, **b** 1000×, **c** 5000×; PVDF-50 at magnifications of **d** 200×, **e** 1000×, **f** 5000×; and PVDF-col at magnifications of **g** 200×, **h** 1000×, **i** 5000×

Moreover, slightly less calcium and phosphorus and more carbon and oxygen were detected in PVDF-col than PVDF-25, potentially indicating a greater amount of carbonate groups.

The mineralization conditions appear to affect the Ca/P molar ratios of the mineralized scaffolds. The Ca/P molar ratios of PVDF-25 and PVDF-col are near 1.9 at all magnifications. On the other hand, the Ca/P molar ratios of PVDF-50 are 2.24, 2.11, and 2.15 at magnifications of 200×, 1000×, and 5000×, respectively, suggesting a greater relative amount of calcium than PVDF-25 and PVDF-col. All three samples exhibit Ca/P molar ratios that reasonably compare to stoichiometric hydroxyapatite (Ca/P = 1.67) [28].

PVDF-50 exhibits a different XRD spectra compared to PVDF-25 and PVDF-col, as shown in Fig. 2. XRD analysis of the unmineralized PVDF shows the characteristic peaks of PVDF at $2\theta = 20.35°$, 36.10°, 41.95°, and 56.60°. These peaks are identified in the XRD results of the mineralized scaffolds as well, along with peaks in between $2\theta = 25.60°–25.95°$ and 31.85°–32.10°, representing the presence of hydroxyapatite. The XRD results of PVDF-25 and PVDF-col are very similar, suggesting that the presence of collagen does not significantly alter the crystal structure of the minerals. However, PVDF-50 is the only sample that displays clear characteristic peaks of calcite (e.g., at $2\theta =$ 23.15°. 29.15°, 39.25°, and 43.00°). Furthermore, the peaks assigned to hydroxyapatite in PVDF-50 are narrower than

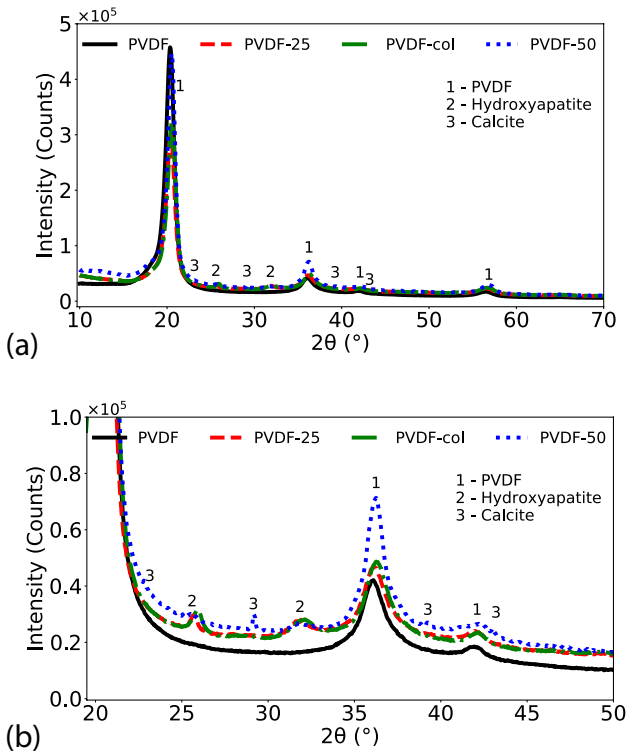

Fig. 2 X-ray diffraction results for unmineralized PVDF, PVDF-25, PVDF-col, PVDF-50 between **a** $2\theta = 10\text{-}70°$ and **b** $2\theta = 20\text{-}50°$

those same peaks in PVDF-25 and PVDF-col, indicating a difference in crystallinity.

Elastic response

The mineralization conditions affect the mechanical properties of the minerals, as indicated by the indentation modulus histograms in Fig. 3a–c. PVDF-25 has an indentation modulus of 0.75 ± 0.58 GPa and indentation hardness of 6.25 ± 5.59 MPa, PVDF-50 has an indentation modulus 7.37 ± 11.87 GPa and indentation hardness of 0.73 ± 2.81 GPa, and PVDF-col has an indentation modulus of 4.91 ± 4.43 GPa and indentation hardness of 0.25 ± 0.21 GPa. PVDF-25 consists of the softest minerals and PVDF-50 consists of the hardest minerals. PVDF-50 has a greater standard deviation of the indentation modulus than mean indentation modulus, which a consequence of the 6% of the tests resulting in an indentation modulus above 20 GPa. These indentation moduli are believed to represent calcite based on the findings in Sect. 3.1 and results in the literature [29, 30]. The enhancement in mechanical properties of PVDF-50 and PVDF-col compared to PVDF-25 agrees with the greater packing density that was observed in the SEM images (Fig. 1).

Statistical deconvolution analysis was performed to provide a greater understanding of the local packing density in PVDF-50 and PVDF-col. The focus was on the indentation

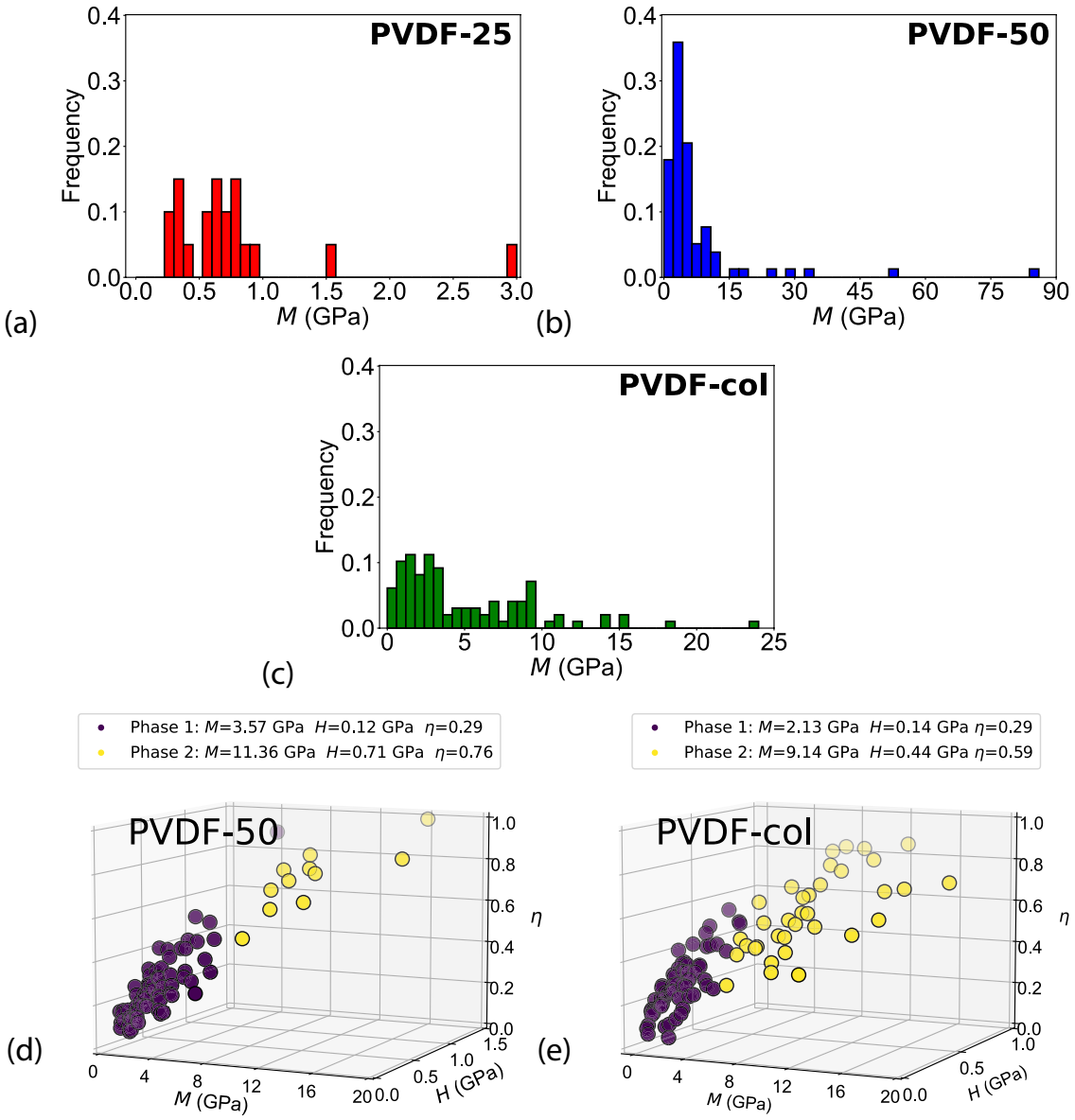

Fig. 3 Indentation modulus, *M*, histograms for **a** PVDF-25, **b** PVDF-50, and **c** PVDF-col; statistical deconvolution analysis of the indentation modulus, hardness, and local packing density data for **d** PVDF-50 and **e** PVDF-col; the purple markers denote the low-density phase and the yellow markers denote the high-density phase

tests corresponding to indentation moduli below 20 GPa, as these are believed to represent the calcium phosphate minerals. In both samples, two distinct phases were identified (Fig. 3d, e). In PVDF-50, the first phase ($M = 3.57$ GPa, $H = 0.12$ GPa, $\eta = 0.29$) comprises 85% of the minerals while the second phase ($M = 11.36$ GPa, $H = 0.71$ GPa, $\eta = 0.76$) comprises 15% of the minerals. In PVDF-col, the first phase ($M = 2.13$ GPa, $H = 0.14$ GPa, $\eta = 0.29$) accounts for 63% of the minerals while the second phase ($M = 9.14$ GPa, $H = 0.44$ GPa, $\eta = 0.59$) accounts for 37% of the minerals. These results suggest that calcium phosphates precipitate into low-density and high-density phases. Furthermore, PVDF-col has the highest packing density, agreeing with the SEM images (Fig. 1).

Fracture behavior

The mineralization protocol for PVDF-50 leads to a significant enhancement in the fracture toughness, while collagen surface treatment leads to potential anisotropy in the fracture response. Figure 4 depicts the fracture scaling curves of the mineralized scaffolds. PVDF-50 has the largest fracture toughness (169.44 ± 28.16 kPa$\sqrt{\text{m}}$), followed by PVDF-col-X1 (47.90 ± 7.14 kPa$\sqrt{\text{m}}$), PVDF-25 (46.63 ± 11.97 kPa$\sqrt{\text{m}}$), and PVDF-col-X2 (40.99 ± 9.30 kPa$\sqrt{\text{m}}$). There does appear to be a slight anisotropy in fracture behavior in PVDF-col, with the fracture toughness being 14% less and more variable in direction X2.

Discussion

In PVDF-50, the higher mineralization temperature and longer duration between refreshing the 10× SBF seem to produce a denser, stiffer, and more fracture-resistant coating of minerals compared to PVDF-25. The higher temperature is believed to improve the density and stiffness of the minerals by enhancing the precipitation and nucleation on the negatively charged surface of the PVDF. Additionally, the higher temperature is believed to enhance the crystallization of calcium phosphates [31]. The presence of calcite in PVDF-50 is attributed to the longer duration between refreshing the 10× SBF based on the results of another study [4]. The calcite is believed to significantly contribute to the higher fracture toughness of PVDF-50 compared to PVDF-25.

Collagen surface treatment is observed to change the size, density, and stiffness of the calcium phosphates minerals that are precipitated at 25 °C. The piezoelectric charge

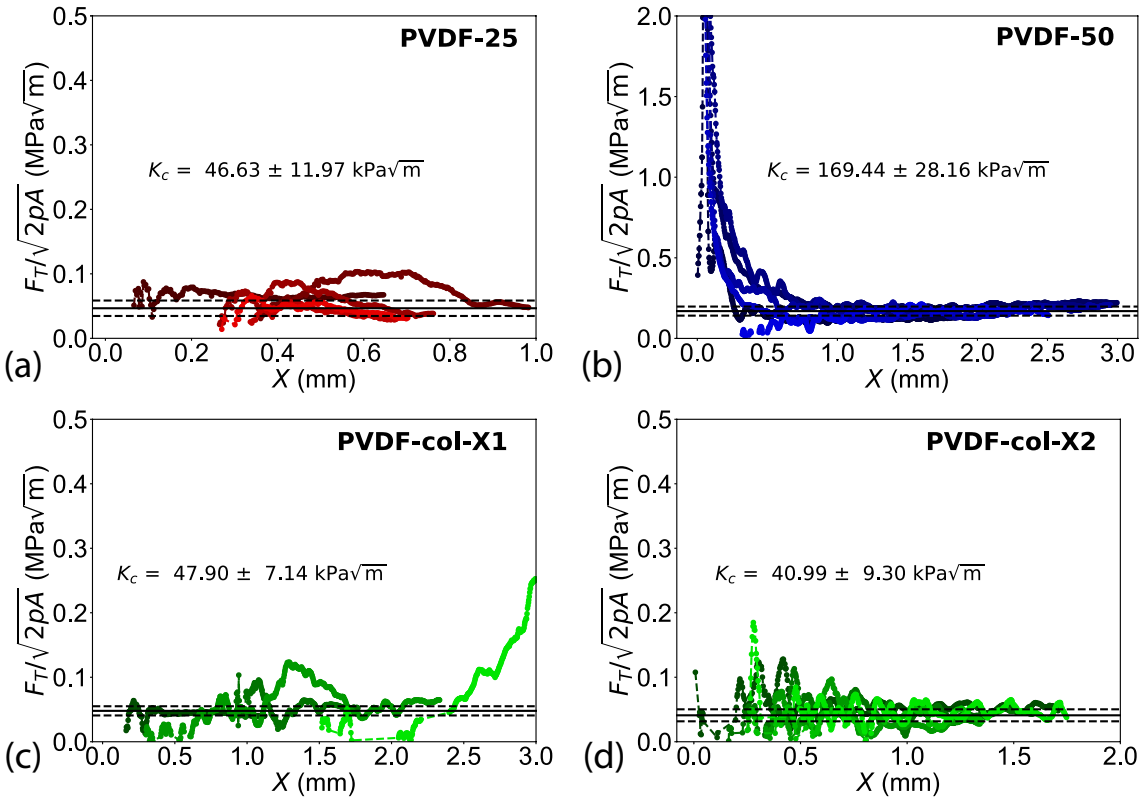

Fig. 4 Fracture scaling curves for **a** PVDF-25, **b** PVDF-50, **c** PVDF-col-X1, and **d** PVDF-col-X2

of PVDF with collagen, which was measured to be over 2 times greater than that of bare PVDF (Table A1 in Supplementary Material), may be the primary reason for the differences between PVDF-col and PVDF-25. Additionally, recent molecular dynamics simulations suggest that calcium phosphate minerals may aggregate near charged surface residues on type I collagen [32]. As such, this could be a reason for the enhanced precipitation and nucleation of calcium phosphates in the presence of collagen.

Conclusions

The influence of the three protocols on the morphology, packing density, elemental composition, Ca/P molar ratio, crystal structure, mechanical properties, and phase distribution of the minerals on piezoelectric PVDF scaffolds was assessed. By increasing the mineralization temperature from 25 to 50 °C, a denser packing was achieved with roughly 10 times the stiffness and 4 times the fracture toughness. By pretreating the PVDF with collagen, the minerals precipitated at 25 °C had a greater packing density, roughly 7 times the stiffness, and potential anisotropy in fracture toughness. Lastly, calcium phosphate minerals were suggested to nucleate in low-density and high-density phases. In future studies, the characteristics of mineralization protocol (e.g., temperature and duration between refreshing the SBF) will be systematically evaluated to enable further control of the microstructure, chemistry, and mechanical properties of the minerals on PVDF.

Supplementary Information The online version contains supplementary material available at https://doi.org/10.1557/s43580-023-00600-7.

Acknowledgments This work made use of the EPIC facility of Northwestern University's NUANCE Center, which has received support from the Soft and Hybrid Nanotechnology Experimental (SHyNE) Resource (NSF ECCS-1542205); the MRSEC program (NSF DMR-1720139) at the Materials Research Center; the International Institute for Nanotechnology (IIN); the Keck Foundation; and the State of Illinois, through the IIN. This work made use of the Hopkins Extreme Materials Institute facility of Johns Hopkins University.

Funding This work was supported by the National Science Foundation under Grant No. DMR 1928702. This work was supported by the National Science Foundation under Grant No. 1747452, which supported Nathanial Buettner in his Ph.D. studies. This work was supported by the Air Force Office of Scientific Research (Award number: FA9550-21-1-0368, Program manager: Dr. Byung-Lip (Les) Lee), the Hanwha Non-Tenured Faculty Award, and the Johns Hopkins University Whiting School of Engineering Start-Up Fund. Any opinions, findings, and conclusions or recommendations expressed in this material are those of the author(s) and do not necessarily reflect the views of the National Science Foundation and the United States Air Force.

Data availability The data will be made available upon request to the corresponding authors.

Declarations

Conflict of interest The authors have no competing interests to declare that are relevant to the content of this article.

References

1. P. Fratzl, J.R. Soc, Interface **4**(15), 637–642 (2007)
2. K. Yamashita, N. Oikawa, T. Umegaki, Chem. Mater. **8**(12), 2697–2700 (1996)
3. P. Zhu, Y. Masuda, K. Koumoto, Biomaterials **25**(17), 3915–3921 (2004)
4. S. Orrego, Z. Chen, U. Krekora, D. Hou, S.Y. Jeon, M. Pittman, C. Montoya, Y. Chen, S.H. Kang, Adv. Mater. **32**(21), 1906970 (2020)
5. M.M. Omar, B. Sun, G. Kitchen, S.H. Kang, J. Compos. Mater. **0021998322112**, 2022 (1858)
6. B. Tandon, J.J. Blaker, S.H. Cartmell, Acta Biomater. **73**, 1–20 (2018)
7. C. Wu, Y. Tang, B. Mao, K. Zhao, S. Cao, Z. Wu, Surf. Coat. Technol. **405**, 126510 (2021)
8. C. Wu, Y. Tang, B. Mao, X. Yan, Y. Pu, K. Zhao, Colloids Surf. B **205**, 111898 (2021)
9. R.V. Chernozem, M.A. Surmeneva, S.N. Shkarina, K. Loza, M. Epple, M. Ulbricht, A. Cecilia, B. Krause, T. Baumbach, A.A. Abalymov, B.V. Parakhonskiy, A.G. Skirtach, R.A. Surmenev, A.C.S. Appl, Mater. and Interfaces **11**(21), 19522–19533 (2019)
10. R.V. Chernozem, M.A. Surmeneva, A.A. Abalymov, B.V. Parakhonskiy, P. Rigole, T. Coenye, R.A. Surmenev, A.G. Skirtach, Mater. Sci. Eng. C **122**, 111909 (2021)
11. Z. Ma, X. Hu, Y. Zhang, X. Li, B. Chen, Q. An, Y. Zhao, Y. Zhang, Eur. J. Chem. **29**(15), e202203166 (2023)
12. T. Gong, T. Li, L. Meng, Y. Chen, T. Wu, J. Zhou, G. Lu, Z. Wang, Ceram. Int. **48**(5), 6461–6469 (2022)
13. V.I. Kalikmanov, *Classical nucleation theory* (Springer, Dordrecht, 2012), p.319
14. Y. Wang, T. Azaïs, M. Robin, A. Vallée, C. Catania, P. Legriel, G. Pehau-Arnaudet, F. Babonneau, M.M. Giraud-Guille, N. Nassif, Nat. Mater. **11**(8), 724–733 (2012)
15. K. Hata, T. Kokubo, T. Nakamura, T. Yamamuro, J. Amer. Ceram. Soc. **78**(4), 1049–1053 (1995)
16. A.C. Tas, S.B. Bhaduri, J. Mater. Res. **19**, 2742–2749 (2004)
17. T. Kokubo, H. Takadama, Biomater. **27**(15), 2907–2915 (2006)
18. A. Oyane, H.M. Kim, T. Furuya, T. Kokubo, T. Miyazaki, T. Nakamura, J. Biomed. Mater. Res. A **65**(2), 188–195 (2003)
19. W.C. Oliver, G.M. Pharr, J. Mater. Res. **7**(6), 1564–1583 (1992)
20. W.C. Oliver, G.M. Pharr, J. Mater. Res. **19**(1), 3–20 (2004)
21. S. Cariou, F.J. Ulm, L. Dormieux, J. Mech. Phys. Solids **56**(3), 924–952 (2008)
22. A.T. Akono, Materials **13**(17), 3837 (2020)
23. F.J. Ulm, M. Vandamme, C. Bobko, J. Alberto Ortega, K. Tai, C. Ortiz, J. Amer. Ceram. Soc. **90**(9), 2677–2692 (2007)
24. G. Constantinides, K.S.R. Chandran, F.J. Ulm, K.J. Van Vliet, Mater. Sci. Eng. A **430**, 189–202 (2006)
25. A.-T. Akono, N.X. Randall, F.-J. Ulm, J. Mater. Res. **27**, 485–493 (2012)
26. A.-T. Akono, F.-J. Ulm, Wear **313**, 117–124 (2014)
27. L.A. Hapach, J.A. VanderBurgh, J.P. Miller, C.A. Reinhart-King, Phys. Bio. **12**(6), 061002 (2015)
28. S.V. Dorozhkin, Prog. Biomater. **5**(1), 9–70 (2016)
29. R. Ševčík, M. Pérez-Estébanez, A. Viani, P. Šašek, P. Mácová, Powder Tech. **284**, 265–271 (2015)

30. Z. Deng, L. Chen, L. Li, J. Mech. Behav. Biomed. Mater. **137**, 105538 (2023)
31. L.M. Rodriguez-Lorenzo, M. Vallet-Regi, Chem. Mater. **12**(8), 2460–2465 (2000)
32. Z. Xue, M. Yang, D. Xu, J. Phys. Chem. C **123**(4), 2533–2543 (2019)